Signal-to-noise properties of correlation plenoptic imaging with chaotic light

Giovanni Scala,[1,2] Milena D'Angelo,[1,3,2] Augusto Garuccio,[1,2] Saverio Pascazio,[1,2,3] and Francesco V. Pepe[2,*]
[1]*Dipartimento Interateneo di Fisica, Università degli Studi di Bari, I-70126 Bari, Italy*
[2]*INFN, Sezione di Bari, I-70125 Bari, Italy*
[3]*Istituto Nazionale di Ottica (INO-CNR), I-50125 Firenze, Italy*

(Received 26 January 2019; published 7 May 2019)

Correlation plenoptic imaging (CPI) is an imaging technique that exploits the correlations between the intensity fluctuations of light to perform the typical tasks of plenoptic imaging (namely, refocusing out-of-focus parts of the scene, extending the depth of field, and performing three-dimensional reconstruction) without entailing a loss of spatial resolution. Here, we consider two different CPI schemes based on chaotic light, both employing ghost imaging: the first one to image the object, the second one to image the focusing element. We characterize their noise properties in terms of the signal-to-noise ratio (SNR) and compare their performances. We find that the SNR can be significantly easier to control in the second CPI scheme involving standard imaging of the object; under adequate conditions, this scheme enables the number of frames for achieving the same SNR to be reduced by 1 order of magnitude.

DOI: 10.1103/PhysRevA.99.053808

I. INTRODUCTION

Plenoptic imaging is a recently established optical imaging technique based on the idea of recording both the spatial distribution and propagation direction of light in a single exposure [1]. Although the first feasible proposal to apply plenoptic imaging to digital cameras dates back to the mid-2000s [2], the seminal intuition can be attributed to Lippmann [3] one century earlier. Plenoptic imaging is currently employed in a very wide range of applications, including stereoscopy [1,4,5], microscopy [6–9], particle image velocimetry [10], particle tracking and sizing [11], and wavefront sensing [12–15]. Since plenoptic devices are able to simultaneously acquire two-dimensional (2D) images from multiple perspectives, they are considered among the fastest and most promising methods for three-dimensional (3D) imaging [16], as shown by the very recent use in imaging of animal neuronal activity [9], surgical robotics [17], endoscopy [18], and blood-flow visualization [19].

Currently available plenoptic imaging devices are based on the intensity measurement on a single detector [2,20,21]. Their key component is a microlens array that produces multiple images of some reference plane, not coinciding with the object plane defined by the main lens. In this way the direction of light from the object plane to such a reference plane can be traced, enabling us to reconstruct (*refocus*) the out-of-focus parts of the scene, extend the depth of field, and perform 3D imaging in postprocessing. However, capturing directional information entails a fundamental tradeoff with the image resolution. In particular, spatial resolution in plenoptic devices cannot reach the diffraction limit, as determined by the light wavelength and the numerical aperture of the imaging system.

Several technologies have been developed in the field of quantum imaging which go beyond the capabilities of standard imaging and interferometry systems [22–30]. Recently, a technique named correlation plenoptic imaging (CPI) [31] has been shown to overcome the typical tradeoff between spatial and directional resolution of plenoptic imaging by exploiting intensity correlations of either chaotic light [32–35] or entangled photon pairs [36]. The key idea of CPI is to encode information of the image and the direction of light in two distinct sensors; the desired information emerges by evaluating intensity correlations. Since two separate sensors are used, the image resolution can reach the diffraction limit. CPI is inspired by ghost imaging with chaotic and entangled light [22,37–46], with a crucial modification: the "bucket" detector, collecting all light that propagates in one optical path in ghost imaging, is replaced by a spatially resolving detector in CPI. The resolution of such a detector enables one to track the direction of light.

Though the tradeoff between spatial and directional resolution can be overcome by using CPI instead of traditional plenoptic imaging, the former has the disadvantage of requiring the reconstruction of the source statistics, thus losing the single-shot advantage of standard plenoptic imaging. The signal-to-noise ratio (SNR) improves with the number of frames; however, to aim at performing real-time imaging, the number of acquired frames should be as small as possible. The choice of the optimal frame number is particularly delicate in the case of ghost images with chaotic light, characterized by a well-known tradeoff between resolution and SNR [47–50]. Ways to mitigate such tradeoff involve image analysis techniques [51,52] and alternative measurement schemes [53]. The objective of this paper is to characterize and compare the SNR in two different CPI schemes based on the properties of chaotic light and designed according to complementary concepts (see Fig. 1): the first one (SETUP1) exploits ghost imaging to obtain the image of the object and standard

*francesco.pepe@ba.infn.it

 ©2019 American Physical Society

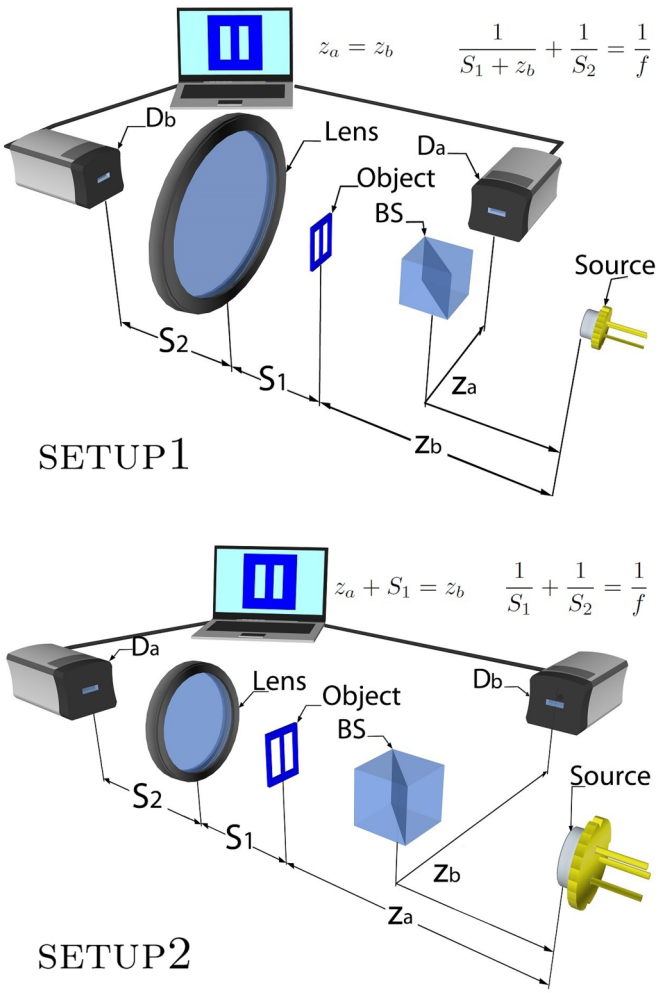

FIG. 1. Schematic representation of two setups that enable plenoptic imaging to be performed by measuring the correlation of intensity fluctuations between points on two spatially resolving detectors D_a and D_b. Both setups are illuminated by chaotic light that is split into two paths by a beam splitter and feature a transmissive object and a lens of focal length f. In SETUP1 (upper panel), the chaotic source is focused by the lens on detector D_b, while the "ghost" image of the object emerges in correspondence of D_a from the average correlation $\Gamma(\boldsymbol{\rho}_a, \boldsymbol{\rho}_b) = \langle \Delta i(\boldsymbol{\rho}_a) \Delta i(\boldsymbol{\rho}_b) \rangle$. SETUP2 (lower panel) is based on a different working principle: the image of the object is formed by the lens on D_a, while the ghost image of the lens is retrieved in correspondence of D_b by computing correlations between D_a and D_b. In both cases, encoding these two images in the correlation function of Eq. (1) provides information on the direction of light in the setup, allowing the possibility to recover the image of the object even if the focusing conditions (namely, $z_b = z_a$ for SETUP1, and $1/S_1 + 1/S_2 = 1/f$ for SETUP2) are not satisfied.

imaging to get directional information, while in the second one (SETUP2) the object is imaged by a lens, and ghost imaging is used to obtain directional information.

In Sec. II, we outline the problem and define its general aspects. In Sec. III, we derive the results that enable one to determine the optimal number of frames to be acquired to achieve the chosen SNR, given the light properties, the optical distances, and the object features. The results obtained in the two setups are compared and interpreted. In Sec. IV, we further discuss the perspectives of this research.

II. CORRELATION PLENOPTIC IMAGING SCHEMES

We consider the two setups (SETUP1 and SETUP2) represented in Fig. 1 for performing correlation plenoptic imaging. These configurations have been proposed in [32] and [34], respectively, and an experimental proof of principle of plenoptic imaging and refocusing in SETUP1 has been performed [35]. The two schemes essentially differ by the way ghost imaging is employed to obtain an image of either the object plane (SETUP1) or the focusing element (SETUP2). The common feature of the two setups is the fact that light emitted by a chaotic source is split in two paths a and b by a beam splitter (BS) and is recorded at the end of each path by the high-resolution detectors D_a and D_b. An object is always placed in one of the two paths. More specifically, intensity patterns $I_A(\boldsymbol{\rho}_a)$ and $I_B(\boldsymbol{\rho}_b)$, with $\boldsymbol{\rho}_{a,b}$ the coordinate on each detector plane, are recorded in time to reconstruct the correlation of intensity fluctuations [40,44],

$$\Gamma_{AB}(\boldsymbol{\rho}_a, \boldsymbol{\rho}_b) = \langle \Delta I_A(\boldsymbol{\rho}_a) \Delta I_B(\boldsymbol{\rho}_b) \rangle, \tag{1}$$

with $\Delta I_{A,B}(\boldsymbol{\rho}_{a,b}) = I_{A,B}(\boldsymbol{\rho}_{a,b}) - \langle I_{A,B}(\boldsymbol{\rho}_{a,b}) \rangle$. The expectation value in (1) must be evaluated over the source statistics, but it can be approximated by the time average of the product of the intensity fluctuations, provided the source is stationary and ergodic [54]. In the discussed setups, the images of the object plane and of the focusing element aperture will be simultaneously encoded in $\Gamma_{AB}(\boldsymbol{\rho}_a, \boldsymbol{\rho}_b)$.

In SETUP1, an image of the object can be obtained only by measuring intensity correlations between D_a and D_b. Along path a (the reflected path in the figure), light directly impinges on detector D_a, placed at an optical distance z_a from the source. In path b (the transmitted path in the figure), a transmissive object lies at a distance z_b from the source. A thin lens of focal length f is placed between the object and the detector D_b at a distance S_1 from the former and S_2 from the latter. Such distances are chosen in order to focus the source on D_b with magnification $M = S_2/(S_1 + z_b)$; hence, they satisfy the thin-lens equation $1/S_2 + 1/(S_1 + z_b) = 1/f$. In the case $z_b = z_a$, measurement of the correlation function $\Gamma_{AB}(\boldsymbol{\rho}_a, \boldsymbol{\rho}_b)$ and direct integration over $\boldsymbol{\rho}_b$ provides the *focused* ghost image of the object [40].

In SETUP2, the image of the lens is recovered from intensity correlations between D_a and D_b. Along path b (the reflected path in figure), light directly impinges on the detector D_b, placed at an optical distance z_b from the source. In path a (the transmitted path in figure), the transmissive object is placed at a distance z_a from the source. The thin lens of focal length f lies between the object and the detector D_a, at a distance S_1 from the former and S_2 from the latter. In this case, the setup is designed to obtain a focused ghost image of the lens on the detector D_b: therefore, distances are fixed in order to satisfy $z_b = z_a + S_1$. The object-to-lens and lens-to-D_a distances are arbitrary. However, it is intuitive that, if $S_2 = S_2^f$ such that $1/S_1 + 1/S_2^f = 1/f$, the image of the object will be sharply focused on D_a.

The refocusing capability of both setups is determined by the fact that the correlation function (1) encodes multiple

coherent images of the object, one for each point $\boldsymbol{\rho}_b$ on D_b. The images corresponding to different pixels on D_b are generally displaced with respect to each other unless a focusing condition is satisfied. In the focused case, integration over detector D_b yields an incoherent image. In the out-of-focus cases, the collected coherent images need to be realigned *before* integrating over D_b, following

$$\Sigma_{\mathrm{ref}}(\boldsymbol{\rho}_a) = \langle \mathcal{S}_{(\alpha,\beta)}(\boldsymbol{\rho}_a)\rangle, \tag{2}$$

with

$$\mathcal{S}_{(\alpha,\beta)}(\boldsymbol{\rho}_a) = \int d^2\boldsymbol{\rho}_b \Delta I_A(\alpha\boldsymbol{\rho}_a + \beta\boldsymbol{\rho}_b)\Delta I_B(\boldsymbol{\rho}_b). \tag{3}$$

The parameters (α, β), that approach (1,0) at focus, are properly chosen to realign the coherent images depending on the setup and read

$$(\alpha,\beta) = \begin{cases} \left(\dfrac{z_a}{z_b}, -\dfrac{1}{M}\left(1-\dfrac{z_a}{z_b}\right)\right) & \text{for SETUP1,} \\ \left(\dfrac{S_2}{S_2^f}, 1-\dfrac{S_2}{S_2^f}\right) & \text{for SETUP2.} \end{cases} \tag{4}$$

It is evident that when the focusing conditions are fulfilled, there is no need to shift and rescale the first argument of Γ, and the high resolution of detector D_b plays no role. In all other cases, the spatial resolution of D_b is essential to reconstruct the image of an out-of-focus object, which, by direct integration over D_b, would appear blurred and degraded.

III. FLUCTUATIONS AND SNR

A. General aspects and statistical model

The objective of this paper is to estimate the signal-to-noise ratio characterizing the refocused images retrieved in SETUP1 and SETUP2. To this end, we shall analyze the fluctuations of the refocused observable $\mathcal{S}_{(\alpha,\beta)}(\boldsymbol{\rho}_a)$, defined in Eq. (3), around its average $\Sigma_{\mathrm{ref}}(\boldsymbol{\rho}_a)$, namely,

$$\begin{aligned}\mathcal{F}(\boldsymbol{\rho}_a) &= \langle \mathcal{S}_{(\alpha,\beta)}(\boldsymbol{\rho}_a)^2\rangle - \langle \mathcal{S}_{(\alpha,\beta)}(\boldsymbol{\rho}_a)\rangle^2 \\ &= \int d^2\boldsymbol{\rho}_{b1} d^2\boldsymbol{\rho}_{b2}\,\Phi(\boldsymbol{\rho}_a, \boldsymbol{\rho}_{b1}, \boldsymbol{\rho}_{b2}),\end{aligned} \tag{5}$$

with Φ determined by the local fluctuations of the intensity correlations [see Eq. (3)]. Let us assume that N_f frames are collected in time to evaluate the expectation value (2). Supposing their statistical independence, the root-mean-square error affecting the evaluation of $\Sigma_{\mathrm{ref}}(\boldsymbol{\rho}_a)$, can be estimated by $\sqrt{\mathcal{F}(\boldsymbol{\rho}_a)/N_f}$. We therefore define the quantity

$$R(\boldsymbol{\rho}_a) = \sqrt{N_f}\,\frac{\Sigma_{\mathrm{ref}}(\boldsymbol{\rho}_a)}{\sqrt{\mathcal{F}(\boldsymbol{\rho}_a)}} \tag{6}$$

as the signal-to-noise ratio. If the collected frames were not statistically independent (e.g., when two or more consecutive frames are collected within the coherence time of the source), the number of frames N_f in Eq. (6) should be replaced by a smaller effective value that takes into account only the nonredundant samples.

A scalar model of the electromagnetic field in which the effects of polarization are neglected will be adopted, and we will assume that the radiation emission by the source is an approximately Gaussian random process, stationary and ergodic. Such a model provides an effective description of a chaotic (pseudothermal) light source in the semiclassical regime, and the quantum corrections to the derived quantities will scale like the inverse number of photons per mode. The scalar approximation of the electromagnetic field is valid whenever the intensity patterns at the output of the optical elements in paths a and b, including the beam splitter, do not depend on polarization, which is always true in our analysis. In particular, the field $V_S(\boldsymbol{\rho}_s)$ at a point $\boldsymbol{\rho}_s$ on the source will be characterized by a Gaussian-Schell equal-time correlator [54],

$$W_S(\boldsymbol{\rho}_s, \boldsymbol{\rho}_s') = \langle V_S(\boldsymbol{\rho}_s)V_S^*(\boldsymbol{\rho}_s')\rangle = I_s e^{-\frac{\rho_s^2}{4\sigma_i^2} - \frac{\rho_s'^2}{4\sigma_i^2} - \frac{(\rho_s-\rho_s')^2}{2\sigma_g^2}}, \tag{7}$$

with I_s the peak intensity, σ_i the width of the intensity profile $\langle I_S(\boldsymbol{\rho}_s)\rangle = W_S(\boldsymbol{\rho}_s, \boldsymbol{\rho}_s) = I_s e^{-\rho_s^2/2\sigma_i^2}$, and σ_g the transverse coherence length on the source plane. Since we are interested in chaotic sources characterized by negligible transverse coherence, we will also approximate the mutual coherence function with a δ function,

$$\exp\left(-\boldsymbol{\rho}^2/2\sigma_g^2\right) \simeq 2\pi\sigma_g^2\delta^{(2)}(\boldsymbol{\rho}), \tag{8}$$

under the integrals. Considering a Gaussian with a finite coherence area σ_g would slightly reduce the resolution of the ghost image, as it would increase the transverse coherence length on the object plane [48]. Such an increase, that scales quadratically with σ_g, can be safely neglected in our setups.

To compute (2) and (5), it is necessary to determine up to eight-point field correlators. Using the Gaussian approximation, we will assume that Isserlis-Wick's theorem [55] is valid for the correlators that involve an equal number of V's and V^*'s, namely,

$$\left\langle \prod_{j=1}^{n} V_S(\boldsymbol{\rho}_j)V_S^*(\boldsymbol{\rho}_j')\right\rangle = \sum_{\mathrm{P}}\prod_{j=1}^{n}\langle V_S(\boldsymbol{\rho}_j)V_S^*(\mathrm{P}\boldsymbol{\rho}_j')\rangle, \tag{9}$$

with P a permutation of the primed indexes, while all other expectation values, including $\langle V\rangle$ and $\langle V^*\rangle$, vanish. Propagation from the source to the detectors along the two paths a and b is deterministic and depends on the transmission functions of the object and the lens. Concerning propagation in free space, a monochromatic field with frequency ω and wave number $k = \omega/c$, evaluated on a plane at a general longitudinal position z, is related to the field at $z_0 < z$ by the paraxial transfer function [56]:

$$V(\boldsymbol{\rho}; z) = \frac{-ik}{2\pi(z-z_0)}\int d^2\boldsymbol{\rho}' V(\boldsymbol{\rho}'; z_0) e^{ik\left[\frac{(\boldsymbol{\rho}-\boldsymbol{\rho}')^2}{2(z-z_0)} + (z-z_0)\right]}. \tag{10}$$

The correlators between fields $V_A(\boldsymbol{\rho}_a)$ and $V_B(\boldsymbol{\rho}_b)$ at the detectors D_a and D_b that determine the refocused image Σ_{ref} and the fluctuation $\mathcal{F}$ thus inherit the factorization property (9) from the fields on the source. In particular, since $I_A = V_A^*V_A$ and $I_B = V_B^*V_B$, the correlation of intensity fluctuations between the two detectors, defined in Eq. (1), reads

$$\Gamma_{AB}(\boldsymbol{\rho}_a, \boldsymbol{\rho}_b) = |\langle V_A(\boldsymbol{\rho}_a)V_B^*(\boldsymbol{\rho}_b)\rangle|^2. \tag{11}$$

Computation of the fluctuation (5), based on the definition (3), also involves the autocorrelations of intensity fluctuations at

the same detector,

$$\Gamma_{DD}(\boldsymbol{\rho}_1,\boldsymbol{\rho}_2) = \langle \Delta I_D(\boldsymbol{\rho}_1)\Delta I_D(\boldsymbol{\rho}_2)\rangle = |\langle V_D(\boldsymbol{\rho}_1)V_D^*(\boldsymbol{\rho}_2)\rangle|^2, \tag{12}$$

with $D = A, B$.

In both setups, $\mathcal{F}(\boldsymbol{\rho}_a)$ is determined with good approximation by the contribution that features only the autocorrelations:

$$\mathcal{F}_0(\boldsymbol{\rho}_a) := \int d^2\boldsymbol{\rho}_{b1}d^2\boldsymbol{\rho}_{b2}\Gamma_{AA}(\alpha\boldsymbol{\rho}_a+\beta\boldsymbol{\rho}_{b1},\alpha\boldsymbol{\rho}_a+\beta\boldsymbol{\rho}_{b2}) \times \Gamma_{BB}(\boldsymbol{\rho}_{b1},\boldsymbol{\rho}_{b2}). \tag{13}$$

Other contributions are typically suppressed as

$$\frac{|\mathcal{F}-\mathcal{F}_0|}{\mathcal{F}_0} \sim \frac{1}{\mathcal{N}_b}, \tag{14}$$

with $\mathcal{N}_b$ the number of transverse modes that propagate towards the detector D_b. Since this quantity determines the number of spatial (in SETUP1) or directional (in SETUP2) resolution cells, it is typically large in a plenoptic imaging setup. Therefore, in the following we shall approximate $\mathcal{F} \simeq \mathcal{F}_0$ when computing the SNR and postpone the full computation of the other contributions to $\mathcal{F}$ to the Appendix.

B. Analysis of SETUP1

Let us first consider SETUP1 (Fig. 1, upper panel). Let us call $A(\boldsymbol{\rho})$ the aperture function of the transmissive object and neglect the finite pupil size of the lens by assuming that it does not affect propagation along path b. Combining free propagation (10) with transmission through the object and the lens [56] and applying the statistical assumptions (7)–(9) on the field correlations at the source, we obtain the correlation between the fluctuations of the intensities $I_A(\boldsymbol{\rho}_a) = |V_A(\boldsymbol{\rho}_a)|^2$ and $I_B(\boldsymbol{\rho}_b) = |V_B(\boldsymbol{\rho}_b)|^2$, which reads

$$\Gamma_{AB}(\boldsymbol{\rho}_a,\boldsymbol{\rho}_b) = |S_{AB}|^4 K_{AB} \times \left|\int d^2\boldsymbol{\rho}_o A(\boldsymbol{\rho}_o) e^{-\gamma_a\left(\frac{\boldsymbol{\rho}_a}{\alpha}-\boldsymbol{\rho}_o\right)^2 - i\gamma_b\boldsymbol{\rho}_b\cdot\boldsymbol{\rho}_o}\right|^2, \tag{15}$$

with $\alpha = z_a/z_b$ as in (4), and the coefficients

$$\gamma_a = \frac{k^2S_{AB}^2}{2z_b^2}, \quad \frac{1}{S_{AB}^2} = \frac{1}{\sigma_i^2} + ik\left(\frac{1}{z_a}-\frac{1}{z_b}\right), \quad \gamma_b = \frac{k}{Mz_b}, \tag{16}$$

while $K_{AB} = K_AK_B$, with

$$K_A = I_s\left(\frac{k\sigma_g}{z_a}\right)^2, \quad K_B = I_s\left(\frac{k^2\sigma_g}{2\pi Mz_b^2}\right)^2. \tag{17}$$

Since γ_a is a generally complex quantity, it will be useful in the following to split it into its real and imaginary parts as $\gamma_a = \gamma_r + i\gamma_i$. The result (15) shows that by varying $\boldsymbol{\rho}_b$, a collection of coherent images of the object is obtained on D_a.

Combining Eq. (15) with the definitions (2)–(4), we determine the refocused image

$$\Sigma_{\mathrm{ref}}(\boldsymbol{\rho}_a) = \frac{\pi}{2\delta^2\gamma_r}|S_{AB}|^4K_{AB}I_\Sigma(\boldsymbol{\rho}_a), \tag{18}$$

with

$$I_\Sigma(\boldsymbol{\rho}_a) = \int d^2\boldsymbol{\rho}_1d^2\boldsymbol{\rho}_2A^*(\boldsymbol{\rho}_a-\boldsymbol{\rho}_1)A(\boldsymbol{\rho}_a-\boldsymbol{\rho}_2)e^{i\frac{\gamma_b(\boldsymbol{\rho}_1^2-\boldsymbol{\rho}_2^2)}{2\delta}} \times \exp\left[-\left(\frac{\gamma_r}{2}+\frac{(\gamma_b-2\delta\gamma_i)^2}{8\delta^2\gamma_r}\right)(\boldsymbol{\rho}_1-\boldsymbol{\rho}_2)^2\right] \tag{19}$$

and $\delta = \beta/\alpha = (1-z_b/z_a)/M$. This quantity is regular in the focused limit $\delta \to 0$, where the $\boldsymbol{\rho}_a$-dependent part of the integral takes the form

$$I_\Sigma(\boldsymbol{\rho}_a)\big|_{z_b=z_a} \sim \int d^2\boldsymbol{\rho}|A(\boldsymbol{\rho}_a-\boldsymbol{\rho})|^2\exp\left(-\frac{\boldsymbol{\rho}^2}{\sigma_A^2}\right), \tag{20}$$

which is exactly the unit-magnification incoherent image obtained in the case of lensless ghost imaging [40,49], whose point-spread function is determined by the squared Fourier transform of the source intensity profile. In the geometrical-optics limit ($k \to \infty$), the dominant contribution to the integral (19) comes from the stationary point of the real and imaginary parts of the exponent, yielding

$$\Sigma_{\mathrm{ref}}^{(g)}(\boldsymbol{\rho}_a) = I_s^2\frac{\pi\sigma_g^4}{\sigma_A^2}|A(\boldsymbol{\rho}_a)|^2, \tag{21}$$

which also shows that Σ_{ref} actually provides a refocused image of the object, characterized by unit magnification.

Let us now evaluate the autocorrelations of the intensity fluctuations,

$$\Gamma_{AA}(\boldsymbol{\rho}_{a1},\boldsymbol{\rho}_{a2}) = \sigma_i^4K_A^2\exp\left(-\frac{(\boldsymbol{\rho}_{a1}-\boldsymbol{\rho}_{a2})^2}{\sigma_A^2}\right), \tag{22}$$

$$\Gamma_{BB}(\boldsymbol{\rho}_{b1},\boldsymbol{\rho}_{b2}) = \sigma_i^4K_B^2\left|\int d^2\boldsymbol{\rho}_1d^2\boldsymbol{\rho}_2A^*(\boldsymbol{\rho}_1)A(\boldsymbol{\rho}_2) \times e^{-\frac{(\boldsymbol{\rho}_1-\boldsymbol{\rho}_2)^2}{2\sigma_B^2}-i\gamma_b(\boldsymbol{\rho}_{b2}\cdot\boldsymbol{\rho}_2-\boldsymbol{\rho}_{b1}\cdot\boldsymbol{\rho}_1)}\right|^2, \tag{23}$$

where

$$\sigma_D = \frac{z_d}{k\sigma_i}, \tag{24}$$

with $D = A, B$, is the transverse coherence length on the planes at a distance $z_d = z_a, z_b$ from the source. The correlation functions (22) and (23) enable us to evaluate the dominant contribution to the variance of the correlation of the intensity fluctuations in Eq. (13), which reads

$$\mathcal{F}_0(\boldsymbol{\rho}_a) = (2\pi)^3\left(K_{AB}\frac{\sigma_A^2\sigma_i^4}{\gamma_b\beta}\right)^2 I_{\mathcal{F}_0}, \tag{25}$$

with

$$I_{\mathcal{F}_0} = \int\left(\prod_{j=1}^{3}d^2\boldsymbol{\rho}_j\right)A(\boldsymbol{\rho}_1)A^*(\boldsymbol{\rho}_2)A(\boldsymbol{\rho}_3)A^*(\boldsymbol{\rho}_1+\boldsymbol{\rho}_3-\boldsymbol{\rho}_2) \times \exp\left(-\frac{(\boldsymbol{\rho}_2-\boldsymbol{\rho}_3)^2}{\sigma_B^2}-\frac{(\boldsymbol{\rho}_1-\boldsymbol{\rho}_2)^2}{2\sigma_i^2(1-z_a/z_b)}\right). \tag{26}$$

The most relevant (and interesting) feature of such a quantity is its independence on the coordinate $\boldsymbol{\rho}_a$ on D_a. Therefore, the signal $\Sigma_{\mathrm{ref}}(\boldsymbol{\rho}_a)$ is noisy and superposed to a further background noise. Such constant background noise stems from the

fact that the intensity profile of the light impinging on D_a is, in the case of SETUP1, not related to the spatial profile of the signal $\Sigma_{\rm ref}(\boldsymbol{\rho}_a)$: actually, as one can easily check, the intensity profile $\langle I_A\rangle$ on D_a is approximately uniform and carries no information on the object transmission function $|A(\boldsymbol{\rho}_a)|^2$.

At this point, the SNR can be exactly evaluated as a function of the number of collected frames by using the results (18)–(25) in expression (6). A useful and intuitive estimate is given by the geometrical-optics approximation of $R(\boldsymbol{\rho}_a)$, which reads

$$R^{(g)}(\boldsymbol{\rho}_a) = \sqrt{2}\pi\sigma_B\sigma_i\left|1-\frac{z_b}{z_a}\right||A(\boldsymbol{\rho}_a)|^2\sqrt{\frac{N_f}{J^{(g)}}}, \tag{27}$$

with

$$J^{(g)} = \int d^2\boldsymbol{\rho}_1 d^2\boldsymbol{\rho}_2 |A(\boldsymbol{\rho}_1)A(\boldsymbol{\rho}_2)|^2 e^{-\frac{(\boldsymbol{\rho}_1-\boldsymbol{\rho}_2)^2}{2\sigma_i^2(1-z_a/z_b)^2}}. \tag{28}$$

Let us first discuss this result in the focused case in which $z_a = z_b$ and $\sigma_A = \sigma_B$. The integrand of (28) becomes localized around $\boldsymbol{\rho}_1 = \boldsymbol{\rho}_2$, and the value of the SNR reduces to

$$R^{(g)}(\boldsymbol{\rho}_a)\big|_{z_b=z_a} = \sqrt{N_f\frac{\pi\sigma_B^2}{\int d^2\boldsymbol{\rho}|A(\boldsymbol{\rho})|^4}}|A(\boldsymbol{\rho}_a)|^2. \tag{29}$$

The above expression highlights the dependence of the SNR on the ratio between the coherence area $\sim\sigma_B^2$ on the object and an "effective area" of the object itself, given by the integral of the $|A|^4$ factor, which is equal to the actual area in the case of binary transmission function. Since the same coherence area determines the resolution through (20), this result entails the well-known tradeoff between resolution and SNR typical of ghost imaging [47–50].

Deep in the out-of-focus regime, when $\sigma_i|1-z_b/z_a|$ becomes larger than the typical size of the object, the exponential modulation under the integral (28) can be neglected, yielding

$$R^{(g)}(\boldsymbol{\rho}_a) \simeq \sqrt{\frac{N_f}{2}}\lambda z_b\left|1-\frac{z_b}{z_a}\right|\frac{|A(\boldsymbol{\rho}_a)|^2}{\int d^2\boldsymbol{\rho}|A(\boldsymbol{\rho})|^2}, \tag{30}$$

with $\lambda = 2\pi/k$ the light wavelength. This expression shows a less trivial dependence on the longitudinal position z_b of the refocused plane but can still be interpreted in terms of the resolution-SNR tradeoff. Actually, as discussed in [32,35], a good estimate of the resolution of the refocused image is given by $\Delta x = (\lambda z_b/a)|1-z_b/z_a|$, where a is the typical linear size of the smallest transmissive parts of the object. Notice, however, that the inverse dependence on the effective area of the object has changed with respect to the focused case (29). As a rule of thumb, we can estimate the SNR of refocused images as

$$\frac{R^{(g)}(\boldsymbol{\rho}_a)}{\sqrt{N_f}} \sim \sqrt{\frac{a^2}{A_{\rm obj}}}\sqrt{\frac{(\Delta x)^2}{A_{\rm obj}}}|A(\boldsymbol{\rho}_a)|^2, \tag{31}$$

a result that depends on the product of the ratios (resolution cell)/(total area) and (smallest detail area)/(total area). In Fig. 2, we show the behavior of the SNR in SETUP1 as a function of the source-to-object distance z_b, comparing the result with the case of a focused ghost image taken with $z_a = z_b$ [Eq. (29)]. The higher SNR of correlation plenoptic imaging is related to the lower resolution of the refocused image with respect to the focused ghost image.

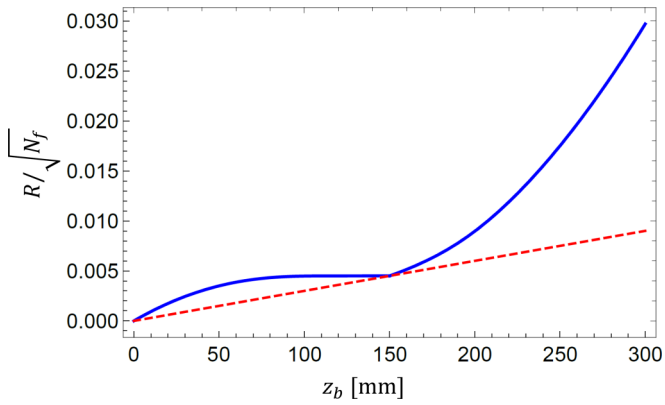

FIG. 2. Signal-to-noise ratio, normalized to the square root of the number of frames, for the refocused image (18) obtained in SETUP1 (solid blue line). The source is characterized by wavelength $\lambda = 532$ nm and a Gaussian intensity profile of width $\sigma_i = 2.5$ mm and is placed at a fixed distance $z_a = 150$ mm from detector D_a. The focused image, obtained at $z_b = z_a$, is characterized by resolution $\Delta x = 10\ \mu$m. The values are computed in correspondence of a totally transmissive point ($A = 1$) of a binary object with transmissive area $A_{\rm obj} = 4$ mm^2. The SNR for a ghost image taken at $z_a = z_b$ as a function of z_b (red dashed line) is shown for comparison.

C. Analysis of SETUP2

In the analysis of SETUP2, we shall consider a finite-size pupil $P(\boldsymbol{\rho})$ of the lens that determines the spatial resolution and assume that the transverse size of the source is asymptotically large, namely, that the finite size of the source does not affect in a relevant way the correlation of the intensity fluctuations. In this way, the most relevant part of the mutual correlation function reads

$$\Gamma_{AB}(\boldsymbol{\rho}_a,\boldsymbol{\rho}_b) = \left(\frac{z_a(z_a+S_1)}{kS_1}\right)^2 K_{AB} \times\left|\int d^2\boldsymbol{\rho}_o A(\boldsymbol{\rho}_o)\tilde{P}_\beta\left(\frac{\boldsymbol{\rho}_o}{S_1}+\frac{\boldsymbol{\rho}_a}{S_2}\right)e^{\frac{ik}{S_1}\boldsymbol{\rho}_o\cdot\boldsymbol{\rho}_b}\right|^2, \tag{32}$$

where

$$\tilde{P}_\beta(\boldsymbol{q}) = \int d^2\boldsymbol{\rho}_\ell P(\boldsymbol{\rho}_\ell)\exp\left(\frac{ik\beta}{2S_2}\boldsymbol{\rho}_\ell^2 - ik\boldsymbol{q}\cdot\boldsymbol{\rho}_\ell\right), \tag{33}$$

which coincides with the Fourier transform of the pupil function, representing the coherent point-spread function (PSF) of the focused image [obtained when $S_2 = S_2^f = (1/f - 1/S_1)^{-1}$ and $\beta = 0$], and $K_{AB} = K_A K_B$, with

$$K_A = I_s\left(\frac{k^3\sigma_g}{(2\pi)^2 S_1 S_2 z_a}\right)^2, \quad K_B = I_s\left(\frac{k\sigma_g}{z_a+S_1}\right)^2. \tag{34}$$

The refocused image, defined by (α,β) in Eq. (4) (second formula), reads

$$\Sigma_{\rm ref}(\boldsymbol{\rho}_a) = \left(\frac{2\pi z_a(z_a+S_1)}{k^2}\right)^2 K_{AB} I_\Sigma(\boldsymbol{\rho}_a), \tag{35}$$

with

$$I_\Sigma(\boldsymbol{\rho}_a) = \int d^2\boldsymbol{\rho}_1 d^2\boldsymbol{\rho}_2 d^2\boldsymbol{\rho}_o P^*(\boldsymbol{\rho}_1)P(\boldsymbol{\rho}_2)e^{-\frac{ik\beta}{2S_2}(\boldsymbol{\rho}_2-\boldsymbol{\rho}_1)^2} \times A^*(\boldsymbol{\rho}_o)A\left(\boldsymbol{\rho}_o + \frac{\beta S_1}{S_2}(\boldsymbol{\rho}_2-\boldsymbol{\rho}_1)\right)e^{ik(\frac{\boldsymbol{\rho}_b}{S_2^f}+\frac{\boldsymbol{\rho}_o}{S_1})(\boldsymbol{\rho}_2-\boldsymbol{\rho}_1)}. \tag{36}$$

One can easily check that in the focused case $\beta = 0$, the above expression reduces to the incoherent image of the transmission function of the object, whose point-spread function is related to the usual square modulus of the Fourier transform of the lens pupil function P. In the general case, the plenoptic imaging property emerges when considering the geometrical-optics limit in which the complicated expression (35) simplifies to

$$\Sigma_{\rm ref}^{(g)}(\boldsymbol{\rho}_a) = I_s^2 \frac{k^2\sigma_g^4}{S_2^2} A_{\rm lens}\left|A\left(-\frac{\boldsymbol{\rho}_a}{\mu}\right)\right|^2, \tag{37}$$

where $\mu = S_2^f/S_1$ is the absolute magnification provided by the lens, and $A_{\rm lens} = \int d^2\boldsymbol{\rho}|P(\boldsymbol{\rho})|^2$ is the (effective) area of the lens.

The autocorrelations, computed in the same regime of large source width σ_i, read

$$\Gamma_{AA}(\boldsymbol{\rho}_{a1},\boldsymbol{\rho}_{a2}) = \left(2\pi K_A \frac{z_a^2}{k^2}\right)^2 \left|\int d^2\boldsymbol{\rho}_o |A(\boldsymbol{\rho}_o)|^2 \times \tilde{P}_\beta\left(\frac{\boldsymbol{\rho}_o}{S_1}+\frac{\boldsymbol{\rho}_{a2}}{S_2}\right)\tilde{P}_\beta^*\left(\frac{\boldsymbol{\rho}_o}{S_1}+\frac{\boldsymbol{\rho}_{a1}}{S_2}\right)\right|^2, \tag{38}$$

$$\Gamma_{BB}(\boldsymbol{\rho}_{b1},\boldsymbol{\rho}_{b2}) = \pi\sigma_i^2 K_B^2\left(\frac{z_a+S_1}{k}\right)^2 \delta^{(2)}(\boldsymbol{\rho}_{b1}-\boldsymbol{\rho}_{b2}). \tag{39}$$

Notice that the autocorrelation on the detector D_b diverges with increasing σ_i; therefore, even if the finite size of the source can become irrelevant for the average correlation of intensity fluctuations, the variance of this quantity crucially depends on it.

Also in this case, the dominant contribution to the variance of $\mathcal{S}_{(\alpha,\beta)}$ can be evaluated by considering the autocorrelations. However, the computation of (13) must take into account the finite size of the detector D_b, since integrating without bounds on $\boldsymbol{\rho}_b$ would yield a divergent result. Since the role of D_b is to detect the ghost image of the lens, which is characterized by unit magnification, the optimal size of this detector is given by the size of the lens. Following these considerations and the result (38), valid in the limit of large source width σ_i, one obtains

$$\mathcal{F}_0(\boldsymbol{\rho}_a) = \pi\sigma_i^2 K_B^2\left(\frac{z_a+S_1}{k}\right)^2 \times \int_{\mathrm{D}_b} d^2\boldsymbol{\rho}_b \Gamma_{AA}(\alpha\boldsymbol{\rho}_a+\beta\boldsymbol{\rho}_b, \alpha\boldsymbol{\rho}_a+\beta\boldsymbol{\rho}_b). \tag{40}$$

In the focused case, the integral in (40) is trivially proportional to $\Gamma_{AA}(\boldsymbol{\rho}_a,\boldsymbol{\rho}_a)$, which is $\boldsymbol{\rho}_a$ dependent, as opposed to the case of SETUP1. In the general case, the analytic evaluation of (40) can become impossible when considering the actual detector area as the integration domain. However, one can perform the computation by regularizing the integral with a Gaussian envelope function $\exp(-\pi\boldsymbol{\rho}_b^2/A_{\mathrm{D}_b})$, where A_{D_b} is the area of detector D_b (or, better, the area of the part of the detector that accommodates the image of the lens).

The geometrical-optics approximation of (40) reads

$$\mathcal{F}_0^{(g)}(\boldsymbol{\rho}_a) = \frac{A_{\mathrm{D}_b}}{4\pi}\left((2\pi)^4\frac{(z_a+S_1)\sigma_i z_a^2 S_2^2}{k^5\left(1-S_2/S_2^f\right)^2}\right)^2 J^{(g)}(\boldsymbol{\rho}_a), \tag{41}$$

with

$$J^{(g)}(\boldsymbol{\rho}_a) = \left[\int d^2\boldsymbol{\rho}_o |A(\boldsymbol{\rho}_o)|^2 \times \left|P\left(\frac{S_2/S_1}{1-S_2/S_2^f}\left(\boldsymbol{\rho}_o+\frac{\boldsymbol{\rho}_a}{\mu}\right)\right)\right|^2\right]^2. \tag{42}$$

The spatial behavior of the variance $\mathcal{F}_0$ is now much less trivial than the constant behavior found in SETUP1. Actually, in the focused limit $S_2 \to S_2^f$, the integrand of (42) becomes infinitely localized around $\boldsymbol{\rho}_o = -\boldsymbol{\rho}_a/\mu$, leading to $J^{(g)}(\boldsymbol{\rho}_a) \propto |A(-\boldsymbol{\rho}_a/\mu)|^4$. This means that, at least in the focused case, *noise is proportional to the signal*. Such a feature is related to the fact that, in this case, the field transmitted by the object is focused on D_a, and this is reflected in all the correlation functions involving D_a. This feature is absent in the focused case of SETUP1 in which the field impinging on D_a extends well beyond the shape of the object and the image emerges only from intensity correlation measurements. In the opposite limit of large defocusing, instead, the spatial dependence of the lens pupil function P under the integral (42) becomes irrelevant, and the result $J^{(g)}(\boldsymbol{\rho}_a) \propto (\int d^2\boldsymbol{\rho}|A(\boldsymbol{\rho})|^2)^2$ implies that the measurement of $\Sigma_{\rm ref}(\boldsymbol{\rho}_a)$ comes with a uniform background noise. However, as we shall presently find, such background is more easily controllable than the one surrounding the ghost image in SETUP1.

Based on the above considerations, the estimate of the SNR based on Eq. (6) is less trivial than in SETUP1, since the denominator depends on $\boldsymbol{\rho}_a$ and shows different spatial behaviors with varying defocusing. The geometrical-optics expression of the SNR reads

$$R^{(g)}(\boldsymbol{\rho}_a) = 2\sigma_B\sqrt{N_f\frac{\pi}{A_{\mathrm{D}_b}J^{(g)}(\boldsymbol{\rho}_a)}}\left(\frac{1-S_2/S_2^f}{S_2/S_1}\right)^2 \times \left|A\left(-\frac{\boldsymbol{\rho}_a}{\mu}\right)\right|^2 \int d^2\boldsymbol{\rho}|P(\boldsymbol{\rho})|^2. \tag{43}$$

In the focused case, the above quantity reduces to the simple expression

$$R^{(g)}(\boldsymbol{\rho}_a)\big|_{S_2=S_2^f} = 2\sigma_B\sqrt{N_f\frac{\pi}{A_{\mathrm{D}_b}}}, \tag{44}$$

a result that does not depend on $\boldsymbol{\rho}_a$, since noise is proportional to the signal. The constant SNR in (44) is essentially the square root of the ratio of the coherence area $\sim\sigma_B^2$ on D_b and the area A_{D_b} of the same detector, which can also be interpreted as (coherence area on the lens)/(area of the lens), in perfect analogy with Eq. (29), after replacing the object

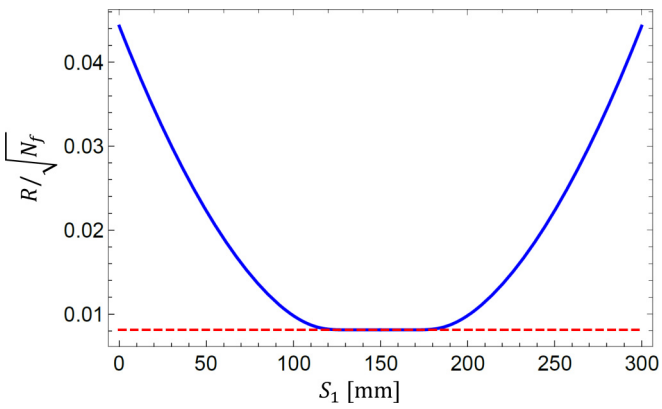

FIG. 3. Signal-to-noise ratio, normalized to the square root of the number of frames, for the refocused image (35) obtained in SETUP2 (solid blue line). The source is characterized by a wavelength $\lambda = 532$ nm and a Gaussian intensity profile of width $\sigma_i = 2.5$ mm, and is placed at a fixed distance $z_b = z_a + S_1 = 300$ mm from the detector D_b. The lens has a focal length $f = 75$ mm and a Gaussian pupil function of width $\sigma_p = 2.5$ mm. Fixing the value $S_2 = 2f = 150$ mm, the focused image, obtained at $S_1 = S_2$, is characterized by the same resolution, depth of field, and magnification as in the case shown in Fig. 2. The values are computed in correspondence of a totally transmissive point ($A = 1$) of a binary object with transmissive area $A_{\rm obj} = 4$ mm^2. The SNR for a ghost image taken at $S_2 = S_2^f = (1/f - 1/S_1)^{-1}$ as a function of S_1 (red dashed line) is shown for comparison.

with the lens. The SNR thus coincides with the one expected for the ghost image of the lens.

In the out-of-focus case, a background noise emerges and the SNR becomes similar in form to (30), yielding

$$R(\boldsymbol{\rho}_a)^{(g)} \simeq 2\sigma_B\sqrt{N_f\frac{\pi}{A_{\mathrm{D}_b}}}\left(\frac{1-S_2/S_2^f}{S_2/S_1}\right)^2 \times \frac{\int d^2\boldsymbol{\rho}|P(\boldsymbol{\rho})|^2}{\int d^2\boldsymbol{\rho}|A(\boldsymbol{\rho})|^2}|P(0)|^2\left|A\left(-\frac{\boldsymbol{\rho}_a}{\mu}\right)\right|^2. \quad (45)$$

The ratio between the area of the lens and the area of the object is generally large for image magnification $\mu \gtrsim 1$, and the SNR also increases quadratically with defocusing, providing a generally more favorable picture compared to SETUP1. A good rule to estimate the order of magnitude of the refocused image SNR thus reads

$$\frac{R^{(g)}(\boldsymbol{\rho}_a)}{\sqrt{N_f}} \sim \left(\frac{S_2/S_1}{1-S_2/S_2^f}\right)^2\sqrt{\frac{\sigma_B^2}{A_{\rm lens}}}\frac{A_{\rm lens}}{A_{\rm obj}}\left|A\left(-\frac{\boldsymbol{\rho}_a}{\mu}\right)\right|^2, \quad (46)$$

where we have assumed that the area of the detector is matched to the area of the lens. In Fig. 3, we represent the behavior of the SNR in SETUP2 as a function of the object-to-lens distance S_1 and compare the result with the case of a focused image taken with $S_2^f = S_2$ (notice that S_2^f is a function of S_1).

D. Summary of the results

We have discussed the properties of the signal-to-noise ratio for SETUP1 and SETUP2, finding that the results obtained for the latter are generally more advantageous than for the former. In the focused case, SETUP2 is characterized by the suppression of background noise that, on the other hand, is a typical feature affecting the ghost image obtained in SETUP1. Moreover, noise in SETUP1 increases with improving resolution on the object, thus entailing a tradeoff between resolution and SNR tradeoff. In the out-of-focus case, background noise is present in both configurations. However, in SETUP1 it depends on small quantities, namely, the ratios $(\Delta x)^2/A_{\rm obj}$ between the area of an effective resolution cell and the total area of the object, and $a^2/A_{\rm obj}$, where the numerator is the area corresponding to the size a of the finest details of the object. In SETUP2, instead we find that the SNR depends also on the ratio $A_{\rm lens}/A_{\rm obj}$, a quantity that is not necessarily small. Therefore, we expect that a smaller number of frames is needed to achieve the same resolution in SETUP2 compared to SETUP1.

To get a quantitative hint of the SNR improvement in SETUP2, we compare the results shown in Figs. 2 and 3, which are referred to two cases that are as homogeneous as possible in terms of resolution, depth of field, and magnification of the focused image. We find that the ratio between the SNR in SETUP2 and SETUP1 at fixed N_f is consistently larger than 1: when such a ratio reaches values around 3.2, for an object placed at $z_b = S_1 = 80$ mm, one-tenth of the frames is needed in SETUP2 to reach the same SNR as in SETUP1. Notice that by considering the expressions (30)–(45), the ratio of the SNRs for out-of-focus images is very weakly dependent on the light wavelength and the area of the object, provided the conditions for the validity of geometrical-optics approximation are satisfied.

IV. CONCLUSIONS AND OUTLOOK

Performing plenoptic imaging by correlation measurements has the potential to improve 3D imaging and microscopy, since it combines high resolution with the possibility to gain directional information. The results obtained in this article provide the experimenter with rules to determine the scaling of the SNR with the number of frames and consequently, to fix the number of frames needed for a fast and accurate imaging of the scene. The problem of optimizing the acquisition time is particularly relevant, both in view of real-time imaging and in all those cases in which additional difficulties in retrieving intensity correlations are present, as it happens when considering unconventional sources like x rays [57,58] to perform CPI. In our future research, we plan to extend our analysis to the case in which CPI is performed with entangled photons [36], investigating whether the remarkable results observed in other kinds of imaging schemes [59–61], in which the shot-noise limit can be overcome, would yield analogous improvements in a setup oriented to plenoptic imaging. Moreover, we will investigate the possibility to combine plenoptic imaging with super-resolution techniques based on correlation imaging with frequency filtering [45,46].

ACKNOWLEDGMENTS

M.D., A.G., and F.V.P. are supported by Istituto Nazionale di Fisica Nucleare (INFN) through the project "PICS." M.D.,

A.G., S.P., and G.S. are supported by Istituto Nazionale di Fisica Nucleare (INFN) through the project "QUANTUM.' A.G. and M.D. are supported by the Italian Ministry of Education, University and Research (MIUR) through project PON Ricerca e Innovazione ARS01_00141.

APPENDIX

We have identified and discussed the term $\mathcal{F}_0$, defined in Eq. (13), as the most relevant term to determine the SNR in both setups. Here we provide the computation of the remaining terms characterizing the local fluctuations $\mathcal{F}(\boldsymbol{\rho}_a)$:

$$\Delta\mathcal{F}(\boldsymbol{\rho}_a) = \mathcal{F}(\boldsymbol{\rho}_a) - \mathcal{F}_0(\boldsymbol{\rho}_a) = \sum_{j=1}^{7} \mathcal{F}_j(\boldsymbol{\rho}_a), \tag{A1}$$

which characterizes the variance at a point $\boldsymbol{\rho}_a$ in the geometrical-optics approximation. In (A1), all but one term are conjugate to each other, namely, $\mathcal{F}_j(\boldsymbol{\rho}_a) = \mathcal{F}^*_{3+j}(\boldsymbol{\rho}_a)$, with $2 \leqslant j \leqslant 4$. The independent contributions read

$$\begin{aligned}\mathcal{F}_1(\boldsymbol{\rho}_a) = &\int d^2\boldsymbol{\rho}_{\mathrm{b}1} d^2\boldsymbol{\rho}_{\mathrm{b}2} \Gamma_{AB}(\alpha\boldsymbol{\rho}_a + \beta\boldsymbol{\rho}_{\mathrm{b}1}, \boldsymbol{\rho}_{\mathrm{b}2}) \\ &\times \Gamma_{AB}(\alpha\boldsymbol{\rho}_a + \beta\boldsymbol{\rho}_{\mathrm{b}2}, \boldsymbol{\rho}_{\mathrm{b}1}),\end{aligned} \tag{A2}$$

$$\begin{aligned}\mathcal{F}_2(\boldsymbol{\rho}_a) = &\int d^2\boldsymbol{\rho}_{b_1} d^2\boldsymbol{\rho}_{b_2} W_{AB}(\alpha\boldsymbol{\rho}_a + \beta\boldsymbol{\rho}_{b_1}, \boldsymbol{\rho}_{b_1}) \\ &\times W_{AB}(\alpha\boldsymbol{\rho}_a + \beta\boldsymbol{\rho}_{b_2}, \boldsymbol{\rho}_{b_2}) \\ &\times W^*_{AB}(\alpha\boldsymbol{\rho}_a + \beta\boldsymbol{\rho}_{b_2}, \boldsymbol{\rho}_{b_1}) \\ &\times W^*_{AB}(\alpha\boldsymbol{\rho}_a + \beta\boldsymbol{\rho}_{b_1}, \boldsymbol{\rho}_{b_2}),\end{aligned} \tag{A3}$$

and

$$\begin{aligned}\mathcal{F}_{3(4)}(\boldsymbol{\rho}_a) = &\int d^2\boldsymbol{\rho}_{\mathrm{b}1} d^2\boldsymbol{\rho}_{\mathrm{b}2} W_{BB}(\boldsymbol{\rho}_{\mathrm{b}1}, \boldsymbol{\rho}_{\mathrm{b}2}) \\ &\times W_{AA}(\alpha\boldsymbol{\rho}_a + \beta\boldsymbol{\rho}_{\mathrm{b}2}, \alpha\boldsymbol{\rho}_a + \beta\boldsymbol{\rho}_{\mathrm{b}1}) \\ &\times W_{AB}(\alpha\boldsymbol{\rho}_a + \beta\boldsymbol{\rho}_{\mathrm{b}1(\mathrm{b}2)}, \boldsymbol{\rho}_{\mathrm{b}1}) \\ &\times W^*_{AB}(\alpha\boldsymbol{\rho}_a + \beta\boldsymbol{\rho}_{\mathrm{b}2(\mathrm{b}1)}, \boldsymbol{\rho}_{\mathrm{b}2}).\end{aligned} \tag{A4}$$

Notice that, in the focused case, both $\mathcal{F}_1$ and $\mathcal{F}_2$ exactly reduce to the squared refocus image Σ^2_{ref}, defined in Eq. (2).

1. Results for SETUP1

The term $\mathcal{F}_1$ reads

$$\mathcal{F}_1(\boldsymbol{\rho}_a) = \left(\frac{\pi}{2\delta^2\gamma_r}\right)^2 |S_{AB}|^8 K^2_{AB} \mathcal{I}_1(\boldsymbol{\rho}_a), \tag{A5}$$

with

$$\mathcal{I}_1(\boldsymbol{\rho}_a) = \int \mathcal{A}_1(\boldsymbol{\rho}_a; \{\boldsymbol{\rho}_i\}) e^{s_1(\{\boldsymbol{\rho}_i\})} \prod_{i=1}^{4} d^2\boldsymbol{\rho}_i, \tag{A6}$$

where $\delta = (1 - z_b/z_a)/M$, S_{AB}, K_{AB}, and $\gamma_r = \mathrm{Re}\gamma_a$ are defined in Eqs. (16) and (17), and

$$\begin{aligned}\mathcal{A}_1(\boldsymbol{\rho}_a; \{\boldsymbol{\rho}_i\}) = &A^*(\boldsymbol{\rho}_a - \boldsymbol{\rho}_1) A(\boldsymbol{\rho}_a - \boldsymbol{\rho}_2) \\ &\times A^*(\boldsymbol{\rho}_a - \boldsymbol{\rho}_3) A(\boldsymbol{\rho}_a - \boldsymbol{\rho}_4),\end{aligned} \tag{A7}$$

$$\begin{aligned}s_1(\{\boldsymbol{\rho}_i\}) = &-\gamma_a\left(\boldsymbol{\rho}_2^2 + \boldsymbol{\rho}_4^2\right) - \gamma_a^*\left(\boldsymbol{\rho}_1^2 + \boldsymbol{\rho}_3^2\right) \\ &+ \frac{R_1^2(\{\boldsymbol{\rho}_i\}) + R_2^2(\{\boldsymbol{\rho}_i\})}{8\delta^2\gamma_r}.\end{aligned} \tag{A8}$$

The functions R_1 and R_2 in (A8) are defined as follows:

$$\begin{aligned}R_1(\{\boldsymbol{\rho}_i\}) = R(\boldsymbol{\rho}_1, \boldsymbol{\rho}_2, \boldsymbol{\rho}_3, \boldsymbol{\rho}_4) = &i\gamma_b(\boldsymbol{\rho}_4 - \boldsymbol{\rho}_3) \\ &- 2\gamma_a\delta\boldsymbol{\rho}_2 - 2\gamma_a^*\delta\boldsymbol{\rho}_1,\end{aligned} \tag{A9}$$

$$R_2(\{\boldsymbol{\rho}_i\}) = R(\boldsymbol{\rho}_3, \boldsymbol{\rho}_4, \boldsymbol{\rho}_2, \boldsymbol{\rho}_1). \tag{A10}$$

In the geometrical-optics limit, the function $\mathcal{F}_1$ in (A5) reduces to

$$\mathcal{F}_1^{(g)}(\boldsymbol{\rho}_a) = \frac{4\pi^6}{\gamma_b^4\gamma_r^2} |S_{AB}|^8 K^2_{AB} |A(\boldsymbol{\rho}_a)|^4. \tag{A11}$$

The term $\mathcal{F}_2$ reads

$$\mathcal{F}_2(\boldsymbol{\rho}_b) = \left(\frac{\pi}{2\delta^2\gamma_r}\right)^2 |S_{AB}|^8 K^2_{AB} \mathcal{I}_2(\boldsymbol{\rho}_a), \tag{A12}$$

with

$$\mathcal{I}_2(\boldsymbol{\rho}_a) = \int \mathcal{A}_1(\boldsymbol{\rho}_a; \{\boldsymbol{\rho}_i\}) e^{s_2(\{\boldsymbol{\rho}_i\})} \prod_{i=1}^{4} d^2\boldsymbol{\rho}_i, \tag{A13}$$

and $\mathcal{A}_1$ is defined in Eq. (A7), while the argument of the exponential reads

$$\begin{aligned}s_2(\{\boldsymbol{\rho}_i\}) = &-\gamma_a\left(\boldsymbol{\rho}_2^2 + \boldsymbol{\rho}_1^2\right) - \gamma_a^*\left(\boldsymbol{\rho}_4^2 + \boldsymbol{\rho}_3^2\right) \\ &+ \frac{R_3^2(\{\boldsymbol{\rho}_i\}) + R_4^2(\{\boldsymbol{\rho}_i\})}{8\delta^2\gamma_r},\end{aligned} \tag{A14}$$

with [see Eq. (A9)]

$$R_3(\{\boldsymbol{\rho}_i\}) = R(\boldsymbol{\rho}_4, \boldsymbol{\rho}_1, \boldsymbol{\rho}_3, \boldsymbol{\rho}_1), \tag{A15}$$

$$R_4(\{\boldsymbol{\rho}_i\}) = R(\boldsymbol{\rho}_3, \boldsymbol{\rho}_2, \boldsymbol{\rho}_4, \boldsymbol{\rho}_2). \tag{A16}$$

The geometrical-optics result is

$$\mathcal{F}_2^{(g)}(\boldsymbol{\rho}_a) = \frac{4\pi^6}{\gamma_b^3\gamma_r(\gamma_b\gamma_r + 4i\delta|\gamma_a|^2)} |S_{AB}|^8 K^2_{AB} |A(\boldsymbol{\rho}_a)|^4. \tag{A17}$$

The terms $\mathcal{F}_3$ and $\mathcal{F}_4$ in Eq. (A4) are both complex and very similar to each other. In this case,

$$\mathcal{F}_{3(4)}(\boldsymbol{\rho}_b) = \frac{\pi^2}{q_1 q_2} |S_{AB}|^4 \sigma_i^4 K^2_{AB} \mathcal{I}_{3(4)}(\boldsymbol{\rho}_a), \tag{A18}$$

with

$$\mathcal{I}_{3(4)}(\boldsymbol{\rho}_a) = \int \mathcal{A}_3(\boldsymbol{\rho}_a; \{\boldsymbol{\rho}_i\}) e^{s_{3(4)}(\{\boldsymbol{\rho}_i\})} \prod_{i=1}^{4} d^2\boldsymbol{\rho}_i, \tag{A19}$$

where

$$\begin{aligned}\mathcal{A}_3(\boldsymbol{\rho}_a; \{\boldsymbol{\rho}_i\}) = &A^*(\boldsymbol{\rho}_a - \boldsymbol{\rho}_1) A(\boldsymbol{\rho}_a - \boldsymbol{\rho}_2) \\ &\times A(\boldsymbol{\rho}_a - \boldsymbol{\rho}_3) A^*(\boldsymbol{\rho}_a - \boldsymbol{\rho}_4)\end{aligned} \tag{A20}$$

coincides, for an object characterized by a real transmission function, with $\mathcal{A}_1$ defined in Eq. (A7), and

$$s_{3(4)}(\{\boldsymbol{\rho}_i\}) = -\gamma_a\boldsymbol{\rho}_3^2 - \gamma_a^*\boldsymbol{\rho}_4^2 - \frac{(\boldsymbol{\rho}_1-\boldsymbol{\rho}_2)^2}{2\sigma_B^2} + \frac{T_{3(4)}(\{\boldsymbol{\rho}_i\})^2}{4q_1} + \frac{1}{4q_2}\left[U_{3(4)}(\{\boldsymbol{\rho}_i\}) + \frac{\beta^2}{2q_1\sigma_A^2}T_{3(4)}(\{\boldsymbol{\rho}_i\})\right]^2, \tag{A21}$$

with

$$T_{3(4)}(\{\boldsymbol{\rho}_i\}) = -2\delta\gamma_a\boldsymbol{\rho}_3 + i\gamma_b(\boldsymbol{\rho}_{3(2)} - \boldsymbol{\rho}_{1(4)}), \tag{A22}$$

$$U_{3(4)}(\{\boldsymbol{\rho}_i\}) = -2\delta\gamma_a^*\boldsymbol{\rho}_4 - i\gamma_b(\boldsymbol{\rho}_{4(1)} - \Delta\boldsymbol{\rho}_3). \tag{A23}$$

The coefficients q_1 and q_2 appearing in Eq. (A21) are defined as

$$q_1 = \frac{\beta^2}{2\sigma_A^2} + \gamma_a\delta^2, \quad q_2 = q_1^* - \frac{\beta^4}{4q_1\sigma_A^4}. \tag{A24}$$

In the geometrical-optics limit, $\mathcal{F}_3$ and $\mathcal{F}_4$ approach the same value, namely,

$$\mathcal{F}_3^{(g)}(\boldsymbol{\rho}_a) = \mathcal{F}_4^{(g)}(\boldsymbol{\rho}_a) = |S_{AB}|^8K_{AB}^2|A(\boldsymbol{\rho}_a)|^4 \times \frac{64i\pi^6\sigma_A^2\sigma_B^2\left(2\delta^2\gamma_a\sigma_A^2+\beta^2\right)}{\gamma_b^2\left(i\beta^4|\gamma_a|^2 - 8\delta^2\gamma_a\sigma_A^4\gamma_v - (2\beta\sigma_A)^2\gamma_u\right)}, \tag{A25}$$

where

$$\gamma_v = \left(2\left|\gamma_a\right|^2\delta - i\gamma_b\gamma_r\right)\gamma_b, \quad \gamma_u = \gamma_v + 2i\delta^2\gamma_a^2\gamma_a^*. \tag{A26}$$

The obtained results are consistent with the order-of-magnitude evaluation in Eq. (14).

2. Results for SETUP2

As in the main text, we will consider a lens with a finite pupil function $P(\boldsymbol{\rho})$ and an asymptotically large source. The term $\mathcal{F}_1$, as defined in (A2), reads

$$\mathcal{F}_1(\boldsymbol{\rho}_a) = \left(\frac{2\pi z_a(z_a+S_1)}{k^2}\right)^4 K_{AB}^2 I_1(\boldsymbol{\rho}_a), \tag{A27}$$

with

$$I_1(\boldsymbol{\rho}_a) = \int d^2\boldsymbol{\rho}_{o1}d^2\boldsymbol{\rho}_{o2}\prod_{j=1}^4 d^2\boldsymbol{\rho}_j\mathcal{A}_1(\boldsymbol{\rho}_{o1},\boldsymbol{\rho}_{o2},\{\boldsymbol{\rho}_i\}) \times \mathcal{P}_1(\{\boldsymbol{\rho}_i\})\exp\left\{ik\left[\frac{\beta}{2S_2}\left(\boldsymbol{\rho}_2^2-\boldsymbol{\rho}_1^2+\boldsymbol{\rho}_4^2-\boldsymbol{\rho}_3^2\right) + \frac{\boldsymbol{\rho}_{o1}}{S_1}(\boldsymbol{\rho}_1-\boldsymbol{\rho}_2) + \frac{\boldsymbol{\rho}_{o2}}{S_1}(\boldsymbol{\rho}_3-\boldsymbol{\rho}_4) + \frac{\boldsymbol{\rho}_a}{S_2^f}(\boldsymbol{\rho}_1-\boldsymbol{\rho}_2+\boldsymbol{\rho}_3-\boldsymbol{\rho}_4) - \frac{\beta}{S_2}(\boldsymbol{\rho}_2(\boldsymbol{\rho}_4-\boldsymbol{\rho}_3)+\boldsymbol{\rho}_4(\boldsymbol{\rho}_2-\boldsymbol{\rho}_1))\right]\right\}, \tag{A28}$$

with $K_{AB} = K_AK_B$ as defined in Eq. (34), $\beta = 1 - S_2/S_2^f$, and

$$\mathcal{A}_1(\boldsymbol{\rho}_{o1},\boldsymbol{\rho}_{o2},\{\boldsymbol{\rho}_i\}) = A^*(\boldsymbol{\rho}_{o1})A\left(\boldsymbol{\rho}_{o1} + \frac{S_1\beta}{S_2}(\boldsymbol{\rho}_4-\boldsymbol{\rho}_3)\right) \times A^*(\boldsymbol{\rho}_{o2})A\left(\boldsymbol{\rho}_{o2} + \frac{S_1\beta}{S_2}(\boldsymbol{\rho}_2-\boldsymbol{\rho}_1)\right), \tag{A29}$$

$$\mathcal{P}_1(\{\boldsymbol{\rho}_i\}) = P^*(\boldsymbol{\rho}_1)P(\boldsymbol{\rho}_2)P^*(\boldsymbol{\rho}_3)P(\boldsymbol{\rho}_4). \tag{A30}$$

The stationary-phase approximation provides the result

$$\mathcal{F}_1^{(g)}(\boldsymbol{\rho}_a) = \left[\frac{S_1S_2K_{AB}}{\beta}\left(\frac{4\pi^2z_a(z_a+S_1)}{k^3}\right)^2\right]^2 \times \int d^2\boldsymbol{\rho}_od^2\boldsymbol{\rho}_\ell\left|A\left(-\boldsymbol{\rho}_o - 2\frac{\boldsymbol{\rho}_a}{\mu}\right)\right|^2|A(\boldsymbol{\rho}_o)|^2 \times |P(\boldsymbol{\rho}_\ell)|^2\left|P\left[\boldsymbol{\rho}_\ell - \frac{S_2}{S_1\beta}\left(\boldsymbol{\rho}_o + \frac{\boldsymbol{\rho}_a}{\mu}\right)\right]\right|^2, \tag{A31}$$

with $\mu = S_2^f/S_1$.

The result for $\mathcal{F}_2$ is

$$\mathcal{F}_2(\boldsymbol{\rho}_a) = \left(\frac{2\pi z_a(z_a+S_1)}{k^2}\right)^4 K_{AB}^2 I_2(\boldsymbol{\rho}_a), \tag{A32}$$

with

$$I_2(\boldsymbol{\rho}_a) = \int d^2\boldsymbol{\rho}_{o1}d^2\boldsymbol{\rho}_{o2}\prod_{j=1}^4 d^2\boldsymbol{\rho}_j\mathcal{A}_2(\boldsymbol{\rho}_{o1},\boldsymbol{\rho}_{o2},\{\boldsymbol{\rho}_i\}) \times \mathcal{P}_2(\{\boldsymbol{\rho}_i\})\exp\left\{ik\left[\frac{\beta}{2S_2}\left(\boldsymbol{\rho}_1^2+\boldsymbol{\rho}_2^2-\boldsymbol{\rho}_3^2-\boldsymbol{\rho}_4^2\right) + \frac{\boldsymbol{\rho}_{o2}}{S_1}(\boldsymbol{\rho}_4-\boldsymbol{\rho}_1) + \frac{\boldsymbol{\rho}_{o1}}{S_1}(\boldsymbol{\rho}_3-\boldsymbol{\rho}_2) + \frac{\boldsymbol{\rho}_a}{S_2^f}(\boldsymbol{\rho}_3+\boldsymbol{\rho}_4-\boldsymbol{\rho}_2-\boldsymbol{\rho}_1) - \frac{\beta}{S_2}(\boldsymbol{\rho}_1(\boldsymbol{\rho}_3-\boldsymbol{\rho}_1)+\boldsymbol{\rho}_2(\boldsymbol{\rho}_4-\boldsymbol{\rho}_2))\right]\right\}, \tag{A33}$$

where

$$\mathcal{A}_2(\boldsymbol{\rho}_{o1},\boldsymbol{\rho}_{o2},\{\boldsymbol{\rho}_i\}) = A^*(\boldsymbol{\rho}_{o1})A\left(\boldsymbol{\rho}_{o1} + \frac{S_1\beta}{S_2}(\boldsymbol{\rho}_2-\boldsymbol{\rho}_4)\right) \times A^*(\boldsymbol{\rho}_{o2})A\left(\boldsymbol{\rho}_{o2} + \frac{S_1\beta}{S_2}(\boldsymbol{\rho}_4-\boldsymbol{\rho}_3)\right), \tag{A34}$$

$$\mathcal{P}_2(\{\boldsymbol{\rho}_i\}) = P(\boldsymbol{\rho}_1)P(\boldsymbol{\rho}_2)P^*(\boldsymbol{\rho}_3)P^*(\boldsymbol{\rho}_4). \tag{A35}$$

The geometrical-optics approximation of (A32) reads

$$\mathcal{F}_2^{(g)}(\boldsymbol{\rho}_a) = \left[\frac{S_1S_2K_{AB}}{\beta}\left(\frac{4\pi^2z_a(z_a+S_1)}{k^3}\right)^2\right]^2 \times \left|A\left(-\frac{\boldsymbol{\rho}_a}{\mu}\right)\right|^2\int d^2\boldsymbol{\rho}_od^2\boldsymbol{\rho}_\ell e^{-i\frac{kS_2}{S_1^2\beta}(\boldsymbol{\rho}_o+\frac{\boldsymbol{\rho}_a}{\mu})^2}|A(\boldsymbol{\rho}_o)^2 \times |P(\boldsymbol{\rho}_\ell)|^2\left|P\left[\boldsymbol{\rho}_\ell - \frac{S_2}{S_1\beta}\left(\boldsymbol{\rho}_o + \frac{\boldsymbol{\rho}_a}{\mu}\right)\right]\right|^2. \tag{A36}$$

Let us finally compute the remaining independent terms $\mathcal{F}_3$ and $\mathcal{F}_4$. Since after the assumption of asymptotically large source, $W_{BB}(\boldsymbol{\rho}_{b1},\boldsymbol{\rho}_{b2}) \propto \delta(\boldsymbol{\rho}_{b1}-\boldsymbol{\rho}_{b2})$, the two terms are incidentally equal to each other and read

$$\mathcal{F}_3(\boldsymbol{\rho}_a) = \mathcal{F}_4(\boldsymbol{\rho}_a) = \left(\frac{2\pi z_a(z_a+S_1)}{k^2}\right)^4 K_{AB}^2 I_3(\boldsymbol{\rho}_a), \quad \text{(A37)}$$

with

$$\begin{aligned} I_3(\boldsymbol{\rho}_a) = \int & d^2\boldsymbol{\rho}_{o1} d^2\boldsymbol{\rho}_{o2} \prod_{j=1}^{4} d^2\boldsymbol{\rho}_j \mathcal{A}_3(\boldsymbol{\rho}_{o1},\boldsymbol{\rho}_{o2},\{\boldsymbol{\rho}_i\}) \\ & \times \mathcal{P}_1(\{\boldsymbol{\rho}_i\}) \exp\Bigg\{ik\Bigg[\frac{\beta}{2S_2}(\boldsymbol{\rho}_2^2-\boldsymbol{\rho}_1^2+\boldsymbol{\rho}_4^2-\boldsymbol{\rho}_3^2) \\ & + \frac{\boldsymbol{\rho}_{o1}}{S_1}(\boldsymbol{\rho}_1-\boldsymbol{\rho}_2) + \frac{\boldsymbol{\rho}_{o2}}{S_1}(\boldsymbol{\rho}_3-\boldsymbol{\rho}_4) \\ & + \frac{\boldsymbol{\rho}_a}{S_2^f}(\boldsymbol{\rho}_3-\boldsymbol{\rho}_4-\boldsymbol{\rho}_2+\boldsymbol{\rho}_1) \\ & - \frac{\beta}{S_2}(\boldsymbol{\rho}_2(\boldsymbol{\rho}_3-\boldsymbol{\rho}_4-\boldsymbol{\rho}_2-\boldsymbol{\rho}_1))\Bigg]\Bigg\}, \end{aligned} \quad \text{(A38)}$$

with $\mathcal{P}_1$ defined in Eq. (A30) and

$$\begin{aligned} \mathcal{A}_3(\boldsymbol{\rho}_{o1},\boldsymbol{\rho}_{o2},\{\boldsymbol{\rho}_j\}) = & A^*(\boldsymbol{\rho}_{o1})|A(\boldsymbol{\rho}_{o2})|^2 \\ & \times A\left(\boldsymbol{\rho}_{o1} - \frac{\beta S_1}{S_2}(\boldsymbol{\rho}_3-\boldsymbol{\rho}_4-\boldsymbol{\rho}_2+\boldsymbol{\rho}_1)\right), \end{aligned} \quad \text{(A39)}$$

the geometrical-optics limit yields

$$\begin{aligned} \mathcal{F}_3^{(g)}(\boldsymbol{\rho}_a) = & \left[\frac{S_1S_2K_{AB}}{\beta}\left(\frac{4\pi^2 z_a(z_a+S_1)}{k^3}\right)^2\right]^2 \\ & \times \left|A\left(-\frac{\boldsymbol{\rho}_a}{\mu}\right)\right|^2 \int d^2\boldsymbol{\rho}_o d^2\boldsymbol{\rho}_\ell |A(\boldsymbol{\rho}_o)|^2 |P(\boldsymbol{\rho}_\ell)|^2 \\ & \times \left|P\left[\boldsymbol{\rho}_\ell - \frac{S_2}{S_1\beta}\left(\boldsymbol{\rho}_o + \frac{\boldsymbol{\rho}_a}{\mu}\right)\right]\right|^2. \end{aligned} \quad \text{(A40)}$$

Also in this case, we find that the terms of $\mathcal{F}$ satisfy the scaling in Eq. (14).

[1] E. H. Adelson and J. Y. Wang, Single lens stereo with a plenoptic camera, IEEE Trans. Pattern Anal. Mach. Intell. **14**, 99 (1992).

[2] R. Ng, M. Levoy, M. Brédif, G. Duval, M. Horowitz, and P. Hanrahan, Light field photography with a hand-held plenoptic camera, Stanford University Computer Science Tech Report CSTR 2005-02 (2005).

[3] G. Lippmann, Épreuves réversibles donnant la sensation du relief, J. Phys. Theor. Appl. **7**, 821 (1908).

[4] S. Muenzel and J. W. Fleischer, Enhancing layered 3D displays with a lens, Appl. Opt. **52**, D97 (2013).

[5] M. Levoy and P. Hanrahan, Light field rendering, in *Proceedings of the 23rd Annual Conference on Computer Graphics and Interactive Techniques* (Association for Computing Machinery, New York, 1996), pp. 31–42.

[6] M. Levoy, R. Ng, A. Adams, M. Footer, and M. Horowitz, Light field microscopy, ACM Trans. Graph. **25**, 924 (2006).

[7] M. Broxton, L. Grosenick, S. Yang, N. Cohen, A. Andalman, K. Deisseroth, and M. Levoy, Wave optics theory and 3-D deconvolution for the light field microscope, Opt. Express **21**, 25418 (2013).

[8] W. Glastre, O. Hugon, O. Jacquin, H. G. de Chatellus, and E. Lacot, Demonstration of a plenoptic microscope based on laser optical feedback imaging, Opt. Express **21**, 7294 (2013).

[9] R. Prevedel, Y.-G. Yoon, M. Hoffmann, N. Pak, G. Wetzstein, S. Kato, T. Schrödel, R. Raskar, M. Zimmer, E. S. Boyden, and A. Vaziri, Simultaneous whole-animal 3D imaging of neuronal activity using light-field microscopy, Nat. Methods **11**, 727 (2014).

[10] T. W. Fahringer, K. P. Lynch, and B. S. Thurow, Volumetric particle image velocimetry with a single plenoptic camera, Meas. Sci. Technol. **26**, 115201 (2015).

[11] E. M. Hall, B. S. Thurow, and D. R. Guildenbecher, Comparison of three-dimensional particle tracking and sizing using plenoptic imaging and digital in-line holography, Appl. Opt. **55**, 6410 (2016).

[12] C. W. Wu, The plenoptic sensor, Ph.D. thesis, University of Maryland, College Park, 2016.

[13] Y. Lv, R. Wang, H. Ma, X. Zhang, Y. Ning, and X. Xu, SU-G-IeP4-09: Method of human eye aberration measurement using plenoptic camera over large field of view, Med. Phys. **43**, 3679 (2016).

[14] C. Wu, J. Ko, and C. C. Davis, Using a plenoptic sensor to reconstruct vortex phase structures, Opt. Lett. **41**, 3169 (2016).

[15] C. Wu, J. Ko, and C. C. Davis, Imaging through strong turbulence with a light field approach, Opt. Express **24**, 11975 (2016).

[16] X. Xiao, B. Javidi, M. Martinez-Corral, and A. Stern, Advances in three-dimensional integral imaging: Sensing, display, and applications, Appl. Opt. **52**, 546 (2013).

[17] A. Shademan, R. S. Decker, J. Opfermann, S. Leonard, P. C. Kim, and A. Krieger, Plenoptic cameras in surgical robotics: Calibration, registration, and evaluation, in *Proceedings of the 2016 IEEE International Conference on Robotics and Automation (ICRA)* (IEEE, New York, 2016), pp. 708–714.

[18] H. N. Le, R. Decker, J. Opferman, P. Kim, A. Krieger, and J. U. Kang, 3-D endoscopic imaging using plenoptic camera, in *CLEO: Applications and Technology* (Optical Society of America, Washington, DC, 2016), Paper AW4O.2.

[19] M. F. Carlsohn, A. Kemmling, A. Petersen, and L. Wietzke, 3D real-time visualization of blood flow in cerebral aneurysms by light field particle image velocimetry, Proc. SPIE **9897**, 989703 (2016).

[20] T. G. Georgiev and A. Lumsdaine, Focused plenoptic camera and rendering, J. Electron. Imaging **19**, 021106 (2010).

[21] T. Georgiev and A. Lumsdaine, The multifocus plenoptic camera, Proc. SPIE **8299**, 829908 (2012).

[22] T. B. Pittman, Y. H. Shih, D. V. Strekalov, and A. V. Sergienko, Optical imaging by means of two-photon quantum entanglement, Phys. Rev. A **52**, R3429 (1995).

[23] M. Genovese, Real applications of quantum imaging, J. Opt. **18**, 073002 (2016).

[24] O. Schwartz, J. M. Levitt, R. Tenne, S. Itzhakov, Z. Deutsch, and D. Oron, Superresolution microscopy with quantum emitters, Nano Lett. **13**, 5832 (2013).

[25] Y. Israel, R. Tenne, D. Oron, and Y. Silberberg, Quantum correlation enhanced super-resolution localization microscopy enabled by a fibre bundle camera, Nat. Commun. **8**, 14786 (2017).

[26] T. Dertinger, R. Colyer, G. Iyer, S. Weiss, and J. Enderlein, Fast, background-free, 3D super-resolution optical fluctuation imaging (SOFI), Proc. Natl. Acad. Sci. USA **106**, 22287 (2009).

[27] G. Barreto Lemos, V. Borish, G. D. Cole, S. Ramelow, R. Lapkiewicz, and A. Zeilinger, Quantum imaging with undetected photons, Nature (London) **512**, 409 (2014).

[28] M. D'Angelo, Y. H. Kim, S. P. Kulik, and Y. Shih, Identifying Entanglement Using Quantum Ghost Interference and Imaging, Phys. Rev. Lett. **92**, 233601 (2004).

[29] G. Scarcelli, Y. Zhou, and Y. Shih, Random delayed-choice quantum eraser via two-photon imaging, Eur. Phys. J. D **44**, 167 (2007).

[30] M. D'Angelo, A. Mazzilli, F. V. Pepe, A. Garuccio, and V. Tamma, Characterization of two distant double-slits by chaotic light second-order interference, Sci. Rep. **7**, 2247 (2017).

[31] F. Di Lena, F. V. Pepe, A. Garuccio, and M. D'Angelo, Correlation plenoptic imaging: An overview, Appl. Sci. **8**, 1958 (2018).

[32] M. D'Angelo, F. V. Pepe, A. Garuccio, and G. Scarcelli, Correlation Plenoptic Imaging, Phys. Rev. Lett. **116**, 223602 (2016).

[33] F. V. Pepe, G. Scarcelli, A. Garuccio, and M. D'Angelo, Plenoptic imaging with second-order correlations of light, Quantum Meas. Quantum Metrol. **3**, 20 (2016).

[34] F. V. Pepe, O. Vaccarelli, A. Garuccio, G. Scarcelli, and M. D'Angelo, Exploring plenoptic properties of correlation imaging with chaotic light, J. Opt. **19**, 114001 (2017).

[35] F. V. Pepe, F. Di Lena, A. Mazzilli, E. Edrei, A. Garuccio, G. Scarcelli, and M. D'Angelo, Diffraction-Limited Plenoptic Imaging with Correlated Light, Phys. Rev. Lett. **119**, 243602 (2017).

[36] F. V. Pepe, F. Di Lena, A. Garuccio, G. Scarcelli, and M. D'Angelo, Correlation plenoptic imaging with entangled photons, Technologies—Open Access Multidisciplinary Engineering Journal **4**, 17 (2016).

[37] A. Gatti, E. Brambilla, M. Bache, and L. A. Lugiato, Ghost Imaging with Thermal Light: Comparing Entanglement and Classical Correlation, Phys. Rev. Lett. **93**, 093602 (2004).

[38] R. S. Bennink, S. J. Bentley, R. W. Boyd, and J. C. Howell, Quantum and Classical Coincidence Imaging, Phys. Rev. Lett. **92**, 033601 (2004).

[39] A. Valencia, G. Scarcelli, M. D'Angelo, and Y. Shih, Two-Photon Imaging with Thermal Light, Phys. Rev. Lett. **94**, 063601 (2005).

[40] G. Scarcelli, V. Berardi, and Y. Shih, Can two-Photon Correlation of Chaotic Light be Considered as Correlation of Intensity Fluctuations? Phys. Rev. Lett. **96**, 063602 (2006).

[41] F. Devaux, K. P. Huy, S. Denis, E. Lantz, and P.-A. Moreau, Temporal ghost imaging with pseudothermal speckle light, J. Opt. **19**, 024001 (2017).

[42] M. D'Angelo and Y. Shih, Quantum imaging, Laser Phys. Lett. **2**, 567 (2005).

[43] J. H. Shapiro and R. W. Boyd, The physics of ghost imaging, Quant. Info. Proc. **11**, 949 (2012).

[44] H. Chen, T. Peng, and Y. Shih, 100% correlation of chaotic thermal light, Phys. Rev. A **88**, 023808 (2013).

[45] J. Sprigg, T. Peng, and Y. Shih, Super-resolution imaging using the spatial-frequency filtered intensity fluctuation correlation, Sci. Rep. **6**, 38077 (2016).

[46] X. H. Chen, F. H. Kong, Q. Fu, S. Y. Meng, and L. A. Wu, Sub-Rayleigh resolution ghost imaging by spatial low-pass filtering, Opt. Lett. **42**, 5290 (2017).

[47] A. Gatti, M. Bache, D. Magatti, E. Brambilla, F. Ferri, and L. A. Lugiato, Coherent imaging with pseudo-thermal incoherent light, J. Mod. Opt. **53**, 739 (2006).

[48] B. I. Erkmen and J. H. Shapiro, Signal-to-noise ratio of Gaussian-state ghost imaging, Phys. Rev. A **79**, 023833 (2009).

[49] M. N. O'Sullivan, Kam Wai Clifford Chan, and R. W. Boyd, Comparison of the signal-to-noise characteristics of quantum versus thermal ghost imaging, Phys. Rev. A **82**, 053803 (2010).

[50] G. Brida, M. V. Chekhova, G. A. Fornaro, M. Genovese, E. D. Lopaeva, and I. R. Berchera, Systematic analysis of signal-to-noise ratio in bipartite ghost imaging with classical and quantum light, Phys. Rev. A **83**, 063807 (2011).

[51] O. Katz, Y. Bromberg, and Y. Silberberg, Compressive ghost imaging, Appl. Phys. Lett. **95**, 131110 (2009).

[52] S. S. Welsh, M. P. Edgar, P. Jonathan, B. Sun, and M. J. Padgett, Multi-wavelength compressive computational ghost imaging, Proc. SPIE **8618**, 86180I-1 (2013).

[53] F. Ferri, D. Magatti, L. A. Lugiato, and A. Gatti, Differential Ghost Imaging, Phys. Rev. Lett. **104**, 253603 (2010).

[54] L. Mandel and E. Wolf, *Optical Coherence and Quantum Optics* (Cambridge University Press, Cambridge, 1995).

[55] L. Isserlis, On a formula for the product-moment coefficient of any order of a normal frequency distribution in any number of variables, Biometrika **12**, 134 (1918).

[56] J. W. Goodman, *Introduction to Fourier Optics* (McGraw-Hill, New York, 1996).

[57] D. Pelliccia, A. Rack, M. Scheel, V. Cantelli, and D. M. Paganin, Experimental X-Ray Ghost Imaging, Phys. Rev. Lett. **117**, 113902 (2016).

[58] R. Schneider, T. Mehringer, G. Mercurio, L. Wenthaus, A. Classen, G. Brenner, O. Gorobtsov, A. Benz, D. Bhatti, L. Bocklage *et al.*, Quantum imaging with incoherently scattered light from a free-electron laser, Nat. Phys. **14**, 126 (2018).

[59] G. Brida, M. Genovese, and I. Ruo Berchera, Experimental realization of sub-shot-noise quantum imaging, Nat. Photon. **4**, 227 (2010).

[60] A. Meda, E. Losero, N. Samantaray, F. Scafirimuto, S. Pradyumna, A. Avella, I. Ruo-Berchera, and M. Genovese, Photon-number correlation for quantum enhanced imaging and sensing, J. Opt. **19**, 094002 (2017).

[61] N. Samantaray, I. Ruo-Berchera, A. Meda, and M. Genovese, Realization of the first sub-shot-noise wide field microscope, Light Sci. Appl. **6**, e17005 (2017).